ACS APPLIED MATERIALS & INTERFACES

www.acsami.org

Research Article

Predicting the Energetics of Hydrogen Intercalation in Metal Oxides Using Acid–Base Properties

Evan V. Miu, Giannis Mpourmpakis,* and James R. McKone*

Cite This: *ACS Appl. Mater. Interfaces* 2020, 12, 44658–44670

Read Online

ACCESS | Metrics & More | Article Recommendations | Supporting Information

ABSTRACT: The ability to predict intercalation energetics from first principles is attractive for identifying candidate materials for energy storage, chemical sensing, and catalysis. In this work, we introduce a computational framework that can be used to predict the thermodynamics of hydrogen intercalation in tungsten trioxide (WO_3). Specifically, using density functional theory (DFT), we investigated intercalation energetics as a function of adsorption site and hydrogen stoichiometry. Site-specific acid–base properties determined using DFT were used to develop linear structure screening models that informed a kernel ridge energy prediction model. These regressions provided a series of hydrogen binding energy predictions across stoichiometries ranging from WO_3 to $H_{0.625}WO_3$, which were then converted to equilibrium potentials for hydrogen intercalation. Experimental validation using cyclic voltammetry measurements yielded good agreement with the predicted intercalation potentials. This methodology enables fast exploration of a large geometric configuration space and reveals an intuitive physical relationship between acidity, basicity, and the thermodynamics of hydrogen intercalation. Furthermore, the combination of theoretical and experimental results suggests $H_{0.500}WO_3$ as a maximum stable stoichiometry for the bronzes that arises from competition with hydrogen evolution rather than the inability of WO_3 to accommodate additional hydrogen. Our experimental results further indicate hydrogen insertion in WO_3 is highly irreversible for low H-stoichiometries, which we propose to be a consequence of the semiconductor-to-metal transition that occurs upon initial H-intercalation. Overall, the agreement between theory and experiment suggests that local acid–base characteristics govern hydrogen intercalation in tungsten trioxide, and this insight can aid the accelerated discovery of redox-active metal oxides for catalytic hydrogenations.

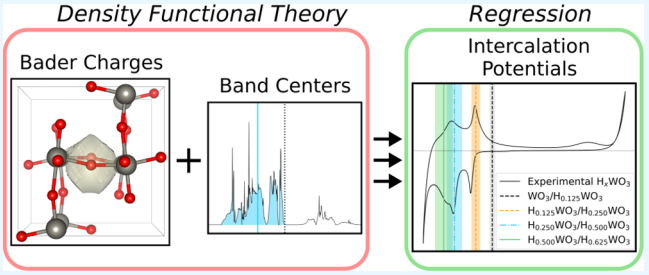

KEYWORDS: *density functional theory, kernel ridge regression, acid, base, PCET, tungsten oxide, hydrogen intercalation*

1. INTRODUCTION

Intercalation is a process where a host material accepts a guest atom into its lattice, subsequently inducing a significant change in material properties. This process is the basis of numerous chemical technologies, including electrochromic devices,[1,2] sensors,[3,4] battery materials,[5,6] and redox catalysis.[7−11] Tungsten trioxide (WO_3) is of particular interest as an intercalation host for its ability to form stable tungsten trioxide bronzes (M_xWO_3) (where M is a metal or hydrogen).[12−14] Our specific interest in WO_3 revolves around its use in redox catalysis, where it has been employed both as a catalyst and a catalyst support. For example, methanol oxidation[7,8] and CO_2 reduction[10,11] have been shown to benefit from the use of WO_3 or a closely related compound. At their core, these reactions involve the net transfer of protons and electrons (i.e., hydrogen equivalents), which implies that the ability of WO_3 to intercalate hydrogen to form hydrogen tungsten bronze (H_xWO_3 where $0 \leq x \leq 0.5$) may be a critical factor in its catalytic properties.

Tungsten oxide bronzes have also been explored for energy storage applications. Aside from hydrogen, WO_3 is also known to intercalate lithium, sodium, and potassium ions upon the application of an electrochemical potential.[15−17] The process of electrochemical intercalation involves coupled cation–electron charge transfer, where electrons are injected into WO_3 along with charge-compensating cation under an appropriately negative electrochemical potential. The reverse deintercalation process proceeds upon application of a positive potential. The rate of H_xWO_3 formation has been shown to be significantly enhanced upon the inclusion of structural water, and $WO_3{\cdot}xH_2O$ can also exhibit both battery-like and pseudocapacitive behaviors.[18,19] This behavior indicates that WO_3 exhibits complex intercalation mechanisms that depend on its precise composition, microstructure, and chemical environment.

Received: June 21, 2020
Accepted: September 15, 2020
Published: September 15, 2020

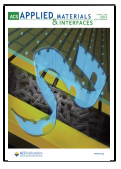

https://dx.doi.org/10.1021/acsami.0c11300
ACS Appl. Mater. Interfaces 2020, 12, 44658–44670

We recently reported that the classical picture of hydrogen spillover—the catalytic hydrogenation of a transition metal oxide—in crystalline WO_3 is mechanistically congruent to electrochemical intercalation, where both can be treated as heterogeneous proton-coupled electron transfer (PCET) reactions.[20] Other work has also demonstrated the ability of WO_3 to engage in simultaneous, spatially separated thermal and electrochemical catalysis, which could confer significant benefits on activity, selectivity, or stability.[21] Together, these results point toward a unified thermodynamic description of the reactivity of hydrogen within metal-oxide hydrogen bronzes like H_xWO_3, which depends on the equilibrium chemical potentials of protons and electrons within the oxide phase.[22]

Considering the inter-relationships between thermochemical and electrochemical reactivity in these systems, the ability to computationally predict the equilibrium potential, U_{eq}, for a wide range of H-intercalation reactions would be valuable for enabling the design of new metal-oxide based hydrogenation catalysts. In this context, hydrogen binding and diffusion in WO_3 have been extensively studied using density functional theory (DFT).[23−27] Much of this work, however, has focused on narrow ranges of H stoichiometries or has not considered the effects of multiple possible atomic configurations of hydrogen within the H_xWO_3 lattice. To build a complete energetic description of hydrogen insertion and uptake, both denser sampling of compositions and specific examination of the bronze configuration space are needed.

Computational methods for predicting the intercalation thermodynamics of metal oxide materials have also been extensively developed in the context of energy storage materials. A common approach involves constructing a convex energy hull by using DFT calculations.[28−30] In this method, multiple structural configurations are investigated for a given stoichiometry, where the lowest-energy state is expected to be representative of the experimentally observed structure. This process is repeated for incremental changes in composition, and all resulting formation energies are placed in the energy-composition plane. A geometric convex hull is then drawn around the array of points, the vertices of which give the stable compositions and the most thermodynamically plausible pathway for the intercalation reaction. Herein, we describe the prediction of proton intercalation in H_xWO_3 by combining DFT calculations with linear and kernel ridge regression (KRR) techniques to decrease the overall computational expense that would normally be required to sample a wide variety of atomic configurations. We have further coupled the computational results with experimental measurements of the H-intercalation potentials for monoclinic WO_3 in aqueous sulfuric acid solution. This combined computational−experimental approach significantly accelerates the process of predicting H-intercalation potentials and provides additional physical insights regarding how the acid−base and redox chemistries of oxide bronze materials are related.

2. COMPUTATIONAL METHODS

Spin-polarized DFT calculations were performed using the Vienna Ab initio Simulation Package (VASP)[31] and all visualizations were performed using VESTA.[32] The projector augmented wave method was used to model the electronic wavefunctions and the Perdew−Burke−Ernzerhof (PBE) functional[33] was used to approximate the exchange−correlation energy. Grimme's D3 correction[34] with Becke−Johnson damping[35] was included to account for dispersion effects. The combination of the PBE functional with the D3 correction has been shown to improve the prediction of tungsten oxide bronze formation energies[36] and metal oxide lattice parameters[37] with respect to uncorrected PBE. Integration of the Brillouin zone was performed using the tetrahedron method with Blöchl corrections.[38] A kinetic energy cutoff of 520 eV was used to construct the plane wave basis set. During geometry relaxations, k-space was sampled using a $3 \times 3 \times 3$ k-point mesh. Electronic energies were converged to variations of less than 1×10^{-6} eV and relaxations were conducted using the conjugate gradient algorithm until all forces became smaller than 0.01 eV/Å.

Periodic calculations were performed using unit cells of WO_3 that contained 8 W atoms, 24 O atoms, and the stoichiometrically relevant number of H atoms. Experimentally determined lattice parameters of monoclinic tungsten trioxide[39] were used to generate the initial, nonintercalated metal oxide structure. Cell shape, volume, and ionic positions in the bare WO_3 were relaxed to find the initial structure for subsequent hydrogen intercalations. Table S1 in the Supporting Information contains the experimental and DFT-relaxed lattice parameters. During structural optimizations of the intercalated H_xWO_3 configurations, the cell shape and volume were kept fixed, whereas all atomic positions were allowed to relax. Bader charge analysis was performed using the Henkelman method.[40] Local and projected electronic density of states (DOS) were generated for each optimized structure using a $5 \times 5 \times 5$ k-point mesh. The occupied and unoccupied electronic band centers were determined from the relevant local, projected DOS.[41]

The binding energies (BEs) of hydrogen within the H_xWO_3 lattice were calculated using the following relationship

$$\Delta E_{j,\mathrm{bind}} = E_{j,\mathrm{H_xWO_3}} - E_{\mathrm{WO_3}} - 4x \cdot E_{\mathrm{H_2}} \quad (1)$$

where $E_{j,\mathrm{H_xWO_3}}$ refers to the electronic energy of the bronze formed by binding a hydrogen at oxygen atom j and x is the ratio of H/W atoms included in the unit cell. $E_{\mathrm{H_2}}$ is the energy of a single diatomic hydrogen molecule. These BEs were used in conjunction with physicochemical descriptors to train the acid−base models.

All regression methods were performed using the scikit-learn package[42] implemented in Python. The structural search models were built around multiple linear regressions. Data were generated from random atomic configurations (i.e., positions of the H atoms within the unit cell) at each investigated H-stoichiometry. Twelve data points were used for training and four were used for validation.

For $H_{0.125}WO_3$, the bare WO_3 lattice has 24 possible intercalation configurations, as given by the 24 O atoms in the unit cell. The lowest energy $H_{0.125}WO_3$ configuration was used as the base geometry for $H_{0.250}WO_3$ calculations; hence, all investigated $H_{0.250}WO_3$ geometries shared the same $H_{0.125}WO_3$ starting configuration. This procedure was continued for higher H-stoichiometries, resulting in a linear model for each investigated level of x in H_xWO_3. More rigorous energy predictions were then generated using a KRR model. A Laplacian kernel with a width of 2.0 was used as the weighting function for the KRR model and the L_2 regularization strength was set to 0.03. Model performance was assessed through mean absolute error (MAE) of validation data computed using 10-fold cross-validation repeated 200 times. We define MAE as $1/n \cdot \sum_i |y_i - x_i|$, where y_i is the model-predicted energy, x_i is the DFT calculated energy, and n is the number of samples.

The site-specific energies predicted using the KRR model were converted to expectation values by weighting and averaging according to the Boltzmann distribution

$$p_j = \frac{e^{-\Delta E_{j,\mathrm{pred}}/k_b \cdot T}}{\sum_k e^{-\Delta E_{k,\mathrm{pred}}/k_b \cdot T}} \quad (2)$$

$$\Delta E_{\mathrm{exp}} = \sum_j p_j \cdot \Delta E_{j,\mathrm{pred}} \quad (3)$$

Confidence intervals on the predicted energies were also computed according to these Boltzmann weightings. The full canonical partition

https://dx.doi.org/10.1021/acsami.0c11300
ACS Appl. Mater. Interfaces 2020, 12, 44658−44670

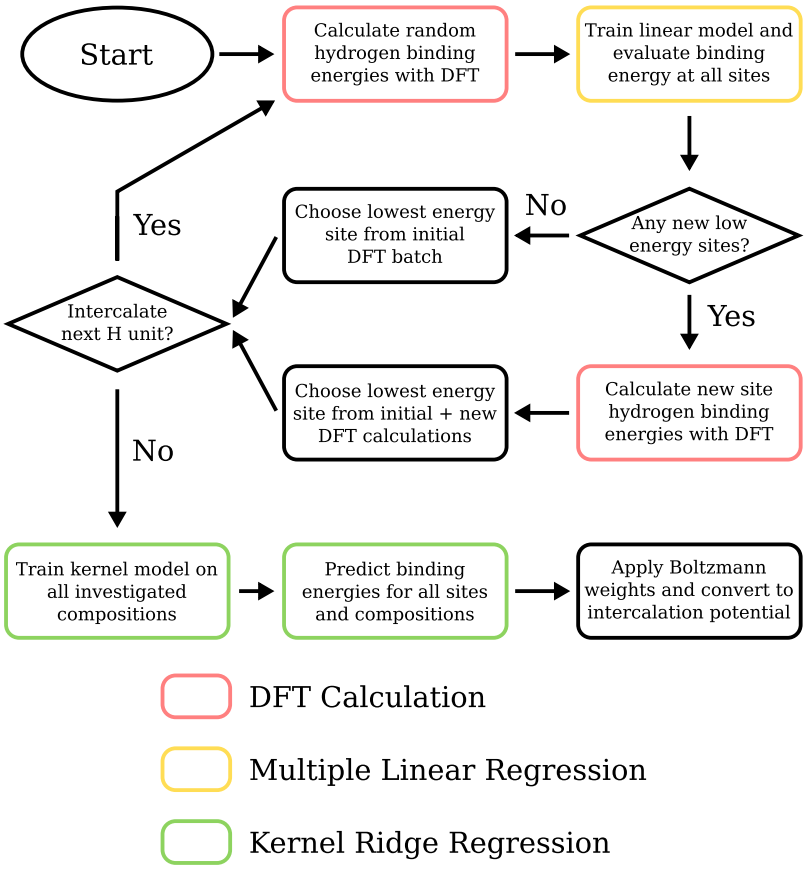

Figure 1. Screening and prediction algorithm used in this work. The goal was to restrict energy predictions to the kernel ridge prediction (green) section, avoiding the expensive DFT (red) sections. This was achieved by accelerating site selection using the linear models (yellow).

function at each stoichiometry was approximated using the $k = 24$ model-predicted energies that resulted from intercalation of the lowest energy configuration from the previous stoichiometry. Model-predicted BE and associated confidence intervals were converted to equilibrium electrochemical potentials for H-intercalation by applying the computational hydrogen electrode (CHE) model[43] to the potential-dependent formation energies of two contiguous stoichiometries

$$\Delta E_{\text{int}} = \Delta E_{\text{H}_{x+\Delta x}\text{WO}_3,\text{expected}} - \Delta E_{\text{H}_x\text{WO}_3,\text{expected}} - 8\Delta x \cdot eU \quad (4)$$

where e is the charge of the electron and U is the applied electric potential. The equilibrium electrochemical hydrogen intercalation potential, U_{eq}, is the value of U that drives ΔE_{int} to zero. This potential can be directly compared to the empirically observed equilibrium potential versus the reversible hydrogen electrode (RHE). This formulation is mathematically identical to that used in the determination of equilibrium voltage via convex hulls.[28] The full algorithm implementing linear screening models and kernel ridge predictions is outlined in Figure 1.

3. EXPERIMENTAL METHODS

Nanoparticulate WO_3 was prepared using a previously reported ion exchange method.[20] All electrochemical characterization was performed using a Gamry Interface 1000 potentiostat in a three-electrode configuration. Counter and reference electrodes were graphite (Electron Microscopy Sciences 0.25 in. diameter, Spectro-Grade) and Ag/Ag^+ (CH Instruments CHI111P), respectively. The working electrode was WO_3 supported on glassy carbon (GC, CH Instruments CHI104P). In a representative deposition of WO_3 onto GC, 0.085 g of the Nafion dispersion (Ion Power, 1100 EW@20 wt % in IPA) was mixed with an equivalent weight of the synthesized WO_3 powder and 100 μL of deionized water (>18 MΩ cm, Millipore Advantage A10). The slurry was sonicated for 20 min, and then 4 μL was deposited onto the GC electrode. An infrared heat lamp was used to dry the sample for 10 min.

After cooling to room temperature, the sample was immersed in 0.5 M H_2SO_4 (aq) electrolyte for electrochemical characterization. The test cell was constructed of borosilicate glass fitted with a custom Teflon cap. A nitrogen purge was used to clear the electrolyte of oxygen before testing and was left running through the duration of each experiment. Cyclic voltammetry (CV) experiments were conducted at a scan rate of 1 mV/s and all scans reported herein were the first cycle observed, unless otherwise indicated. The working electrode was thoroughly cleaned and coated with a fresh film after each voltammogram was recorded. Electrochemical impedance spectroscopy (EIS) was performed in an identical cell setup. Measurements were taken at DC potentials of +0.45, +0.30, +0.15, and 0.00 V versus RHE with an AC modulation of ±10 mV. Each sample was prepolarized at the relevant DC potential for 5 min prior to the start of EIS data collection. The investigated frequency range was 10 mHz to 100 kHz, moving from high to low frequencies. Data were fit in the complex plane using a Randles circuit that included a Warburg impedance unit in series with a charge-transfer resistance.

4. RESULTS AND DISCUSSION

Prior reports of hydrogen intercalation into tungsten trioxide have resulted in widely variable observations and interpretations.[18,19,44−47] Crystal structure, particle morphology, substrate, and electrolyte composition all influence the characteristics of resulting voltammetry measurements. We focused on the monoclinic crystal structure because it is thermodynamically stable under ambient conditions and the most commonly observed polymorph. The ion-exchange synthesis method employed here produces a disk-shaped nanomaterial that we

https://dx.doi.org/10.1021/acsami.0c11300
ACS Appl. Mater. Interfaces 2020, 12, 44658−44670

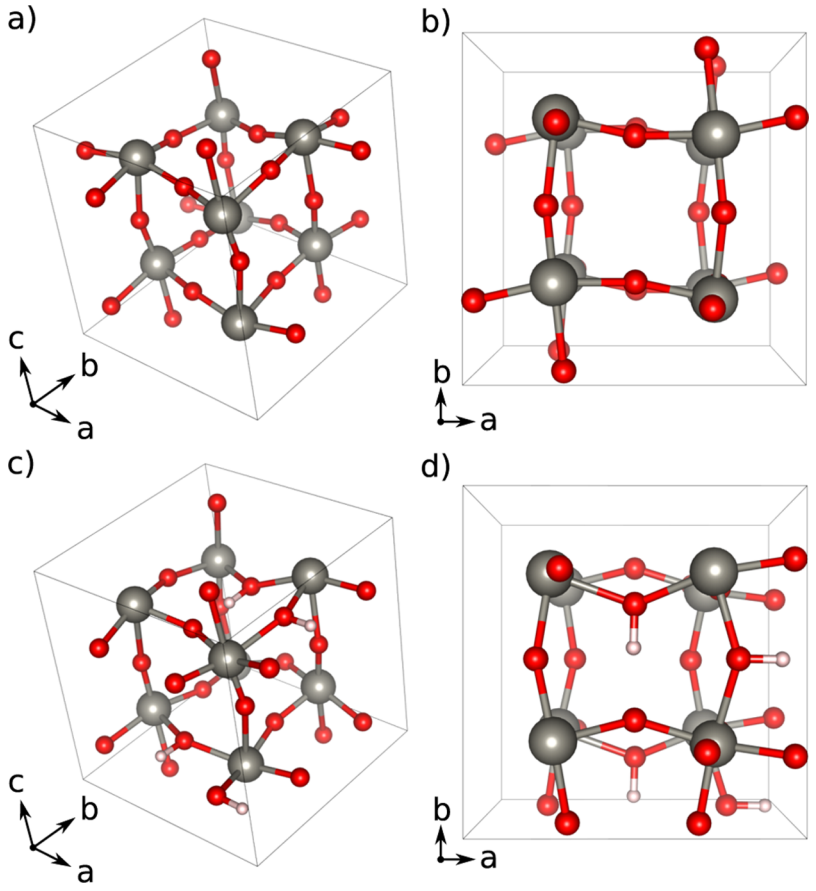

Figure 2. Representative schematics of H_xWO_3 at two different degrees of H intercalation: (a) isometric view and (b) (001) zone axis view of the WO_3 unit cell; (c) isometric; and (d) (001) zone axis view of the lowest energy configuration of the $H_{0.500}WO_3$ unit cell.

previously characterized in detail using X-ray diffraction (XRD), scanning electron microscopy, and high-resolution transmission electron microscopy.[20] The high aspect ratio of these disks helps to minimize the distance over which H-equivalents diffuse in the bulk, resulting in improved resolution of intercalation features in CV. Figure S1 in the Supporting Information further demonstrates the benefit of using nanoparticulate WO_3 rather than dense WO_3 prepared by thermal oxidation of W foils.

Figure 2 shows isometric and (001) zone-axis views of the bulk WO_3 model used in this work. $H_{0.500}WO_3$ is also shown to demonstrate the binding locations of hydrogen atoms as well as the associated lattice distortion. The depicted H positions reflect the most exothermic H binding sites, as discussed in detail below.

In principle, generating a rigorous convex energy hull requires the evaluation of every possible atomic configuration for a given composition. Within the framework of DFT, this approach would pose a prohibitive computational cost if attempted for every configuration. For example, Figure 2a shows that a single unit cell of WO_3 has 8 W atoms and 24 O atoms. Even when considering that hydrogen would be expected to bind to the lattice oxygens to form hydroxyl groups;[25,27,48] a single H atom insertion into the unit cell has at least 24 possible configurations. Accordingly, not considering symmetries or degeneracies, the number of potential configurations is generally described by the combination 24-choose-x ($_{24}C_x$), where x is the number of H atoms in a unit cell of W. This rapidly grows to an intractable problem for direct computation via DFT: for the stoichiometry of $H_{0.500}WO_3$, there exist up to $_{24}C_4$ (10,626) possible atomic configurations within the unit cell.

This issue is commonly remedied by employing the cluster expansion method to approximate the energies for viable configurations of the intercalated material.[49,50] DFT calculations are used to fit the expansion and find the effective cluster interactions, which further enable the determination of relevant thermodynamic quantities using Monte Carlo simulations. Cluster expansion highlights the geometric effects of bulk intercalation on system energy; however, it provides limited information about the relationship between chemical properties and system energy. In an effort to elucidate the relationship between intuitive chemical properties and intercalation energies, we instead applied regression methods commonly used in data science.[51] By doing so, we accelerated the configurational-space search similarly to cluster expansion, while also retaining the ability to describe the underlying physics of the H-intercalation process in WO_3.

Constructing such a model from DFT calculations requires first selecting appropriate descriptors—readily calculable properties of the associated compounds that can then be used to estimate the property of interest via regression models. We chose to use descriptors of the acid−base character of metal oxides, which are widely understood to influence their catalytic activity[52−57] and also bear strongly on the thermochemistry of PCET processes.[58] Consequently, we expected the intercalation of hydrogen into bulk WO_3 to exhibit a strong relationship between local acid−base character

https://dx.doi.org/10.1021/acsami.0c11300
ACS Appl. Mater. Interfaces 2020, 12, 44658−44670

and site-specific hydrogen BE. Mathematically, we represent this relationship as follows

$$\Delta E_{j,\mathrm{est}} = \beta_0 + \sum_i \beta_i x_i \tag{5}$$

In eq 5, the features, x_i, quantify the acidity or basicity of an individual site and the coefficients, β_i, are a series of parameters that can be fit to training data using linear regression.

This formulation describes the screening portion of our approach, where we investigated the candidate descriptors listed in Table 1. These metrics represent various interpretations of local acidity and basicity. Each quantity was calculated for a given site, j. Items labeled "before" were calculated before intercalation, and those labeled "after" were calculated after intercalation occurs at that site. Bader charges were referenced to the number of valence electrons considered for each atom type. The p-band centers were computed for occupied states, and d-band centers were computed for unoccupied states. Standard deviations (σ) for charges and centers were determined from all 24 site quantities resulting from intercalation at site j. These screening models were constructed individually for each level of stoichiometry to guide the search for the most exothermic configuration. This lowest energy binding site was then used as the starting geometry for the binding of additional hydrogen to iteratively generate the next stoichiometric unit and ultimately to outline the convex energy hull for H_xWO_3.

Table 1. All Acid−Base Properties Explored as Model Features in This Work

Bader charges	projected band centers
$O_{j,\mathrm{before}}$	$\epsilon_{p,j,\mathrm{before}}$
$O_{j,\mathrm{after}}$	$\epsilon_{p,j,\mathrm{after}}$
$W_{j,\mathrm{before}}$	$\epsilon_{d,j,\mathrm{before}}$
$W_{j,\mathrm{after}}$	$\epsilon_{d,j,\mathrm{after}}$
$\sigma O_{j,\mathrm{after}}$	$\sigma\epsilon_{p,j,\mathrm{after}}$
$\sigma W_{j,\mathrm{after}}$	$\sigma\epsilon_{d,j,\mathrm{after}}$

Two classes of acid−base quantities were investigated—the first was Bader charge (O_j and W_j in Table 1). The Bader charge directly accounts for electron populations, making it a potential descriptor for Lewis acidity and basicity. Considering intercalation on a generic lattice oxygen site, O_j, the first two descriptors in the first column of Table 1 correspond to the Bader charge of O_j before and after intercalation. Those O sites are also coordinated by two lattice W atoms; the W contributions were, therefore, computed as the average Bader charge of these neighboring atoms. Finally, perturbations in electron density caused by the introduction of hydrogen were quantified through the standard deviation, σ, of the Bader charges for all O or W atoms in the unit cell. Lower values correspond to a more homogeneous distribution of charge, whereas higher values indicate more heterogeneity. Only the post-intercalation σ was considered because σ is a statistic describing all individual sites; hence, a given configuration has only one σ. The value of σ, however, did change depending on the specific site(s) at which hydrogen binds because each hydrogen perturbs the oxide electronic structure differently at each site.

The relationship between DFT-calculated hydrogen BE and the values of σ for the resulting oxides is shown in Figure S2.

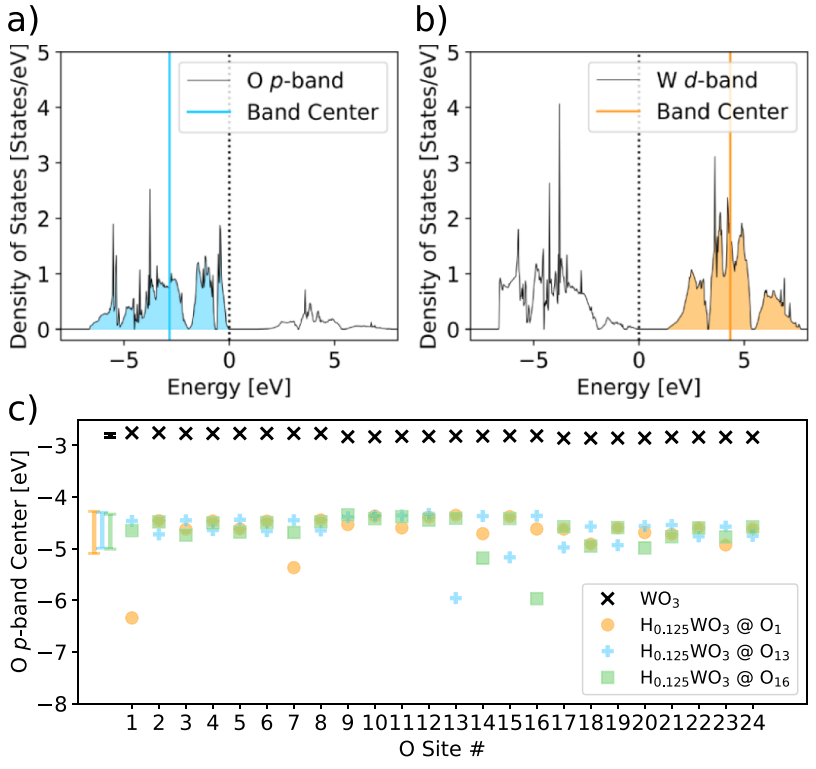

Figure 3. Representative data compiling calculations associated with electronic DOS: (a) calculated oxygen p-band centers associated with site basicity; (b) calculated tungsten d-band centers associated with site acidity; (c) variation in the oxygen p-band center across all the oxygen atoms in the unit cell of WO_3 and three $H_{0.125}WO_3$ examples that vary based on the position of a single H atom in the unit cell. Vertical error bars near the left axis show $\pm 1\sigma$ for each group, centered around the respective means.

https://dx.doi.org/10.1021/acsami.0c11300
ACS Appl. Mater. Interfaces 2020, 12, 44658−44670

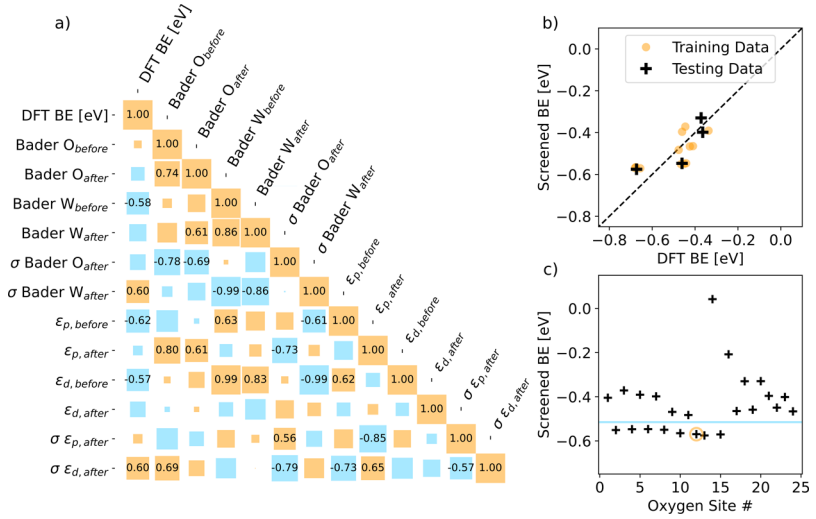

Figure 4. Data used to construct and evaluate linear relationships between acid−base properties and hydrogen BE, shown here for the formation of $H_{0.250}WO_3$. (a) Pearson correlation coefficient (PCC) matrix for pairings of acid−base features and BE, with coefficient values only shown for those considered significant (>0.55 or <−0.55). (b) Parity plot showing the linear screening model performance after training on data from DFT calculations. (c) Model-predicted BE for each site in the $H_{0.125}WO_3$ lattice for hydrogen BE. The solid line indicates the threshold for conducting an additional explicit DFT calculation to confirm site BE. Although the linear model predictions do not directly identify the most exothermic site according to DFT calculations (circled), they do help accelerate its identification.

We observed the general trend that more heterogeneous (larger σ) systems have less exothermic BE, suggesting that more homogeneous (smaller σ) systems are more stable. Therefore, the degree of homogeneity can be viewed as a proxy for bulk material stability, with more homogeneous materials being more stable and vice versa because of increased symmetry.

The second class of descriptors we used comprise the local, projected electronic DOS. Specifically, the projected band centers (ϵ) were used to quantify the energetic positioning of the electrons involved in bonding. Whereas Bader charge tracks the charge density at each site, the electronic DOS gives information on the propensity for a site to engage in an electron transfer, similar to molecular orbital or hard-soft acid base theory.[59−61] For example, occupied oxygen p-band centers and unoccupied aluminum s-band centers have previously been shown to correlate with acidity and dissociative hydrogen binding on γ-alumina surfaces.[41] We similarly examined the occupied p-band centers, ϵ_p, of the oxygen atoms. Higher values of ϵ_p are closer to the Fermi level, E_f, and more likely to donate electrons; therefore, they can be considered more basic.

To characterize DOS contributions from tungsten, we examined the unoccupied d-band centers, ϵ_d, of the W atoms coordinating the O sites of interest. This selection was motivated by the results shown in Figure S3, where decomposing the total DOS for a representative W atom revealed that low-lying unoccupied states have nearly 100% d-band character. Lower values of ϵ_d are closer to E_f and more likely to accept electrons; accordingly, they can be considered more acidic. Similar to our treatment of Bader charges, ϵ_p and ϵ_d were determined for an adsorption site before and after intercalation, and standard deviations of the band centers in the resulting oxide were also calculated to evaluate homogeneity of the bulk cell bands.

To further illustrate the use of acid−base descriptors to determine the energetic consequences of H-intercalation in H_xWO_3, Figure 3 visualizes the DOS metrics used to quantify O site acidity and basicity. Figure 3a,b demonstrate the positioning of representative projected O p-band and W d-band centers with respect to the Fermi level; these quantify basicity and acidity, respectively. Manual inspection of the results of these calculations showed that although the hydrogen atom bonds to oxygen in WO_3, the resulting electron redistribution affects the W d-band. Figure S4 demonstrates how intercalation to $H_{0.125}WO_3$ causes the unoccupied d-states for a representative W atom to shift down and resemble a degenerate semiconductor. With the proton binding to lattice oxygen and the associated electron populating the d-band, both the oxygen and tungsten contributions to adsorption sites are relevant to binding energetics.

We note that GGA exchange−correlation functionals typically underperform at predicting the electronic structure of semiconducting materials, with a significant underestimation of the electronic band gap. Improved results can be attained from the use of a Hubbard U correction or moving to higher levels of theory, such as using hybrid functionals. Figure S4 further compares the W d-projected DOS between PBE-D3 and the hybrid HSE06[62] functional to examine the potential deviations of the GGA approach. In the context of this work, it is important to note the absolute values of the predicted band centers and Bader charges are not quantitatively significant to the resulting energy predictions. What remains critical to the generation of an accurate model is the gradient of the relationship between the descriptor and the prediction target. This is because the regression models employ a free-floating intercept that can correct for constant offsets in the underlying data. Figure S4 clearly shows that the major difference between PBE-D3 and HSE06 electronic structures is a constant offset in band positions, whereas the shape of the DOS does not change very much between functionals. As a result, PBE-D3 seems to be sufficient in capturing the general character of the electronic bands. Considering also the accurate energies returned by PBE-D3 for the WO_3 system,[36,37] we conclude that the

https://dx.doi.org/10.1021/acsami.0c11300
ACS Appl. Mater. Interfaces 2020, 12, 44658−44670

Table 2. Linear Model Coefficients for Each Change in the H/W Ratio

parameter	descriptor	$H_{0.125}WO_3$	$H_{0.250}WO_3$	$H_{0.375}WO_3$	$H_{0.500}WO_3$	$H_{0.625}WO_3$
β_0	intercept	−117.204	7.751	7.784	−15.682	−14.288
β_1	$\epsilon_{p,j,before}$	0.577	−0.333	−0.487	−0.402	0.054
β_2	$\epsilon_{d,j,before}$	−0.577	0.322	2.639	3.204	5.005
β_3	$W_{j,before}$	44.743	−3.997	−6.801	1.744	0.290

selected GGA level of theory is acceptable for building the training and validation data sets.

Figure 3c shows the effects of inserting the first unit of hydrogen into the unit cell of WO_3. Prior to intercalation, the p-band centers of O atom sites are essentially indistinguishable from one another, which reflects the homogeneity and symmetry of the bare oxide. The results of binding hydrogen to three different sites—thereby generating three $H_{0.125}WO_3$ polymorphs designated O_1, O_{13}, and O_{16}—are also shown. After hydrogen uptake, all of the O p-band centers within the oxide are shifted more negative, indicating decreased site basicities. These bands are stabilized with respect to the initial empty lattice and become less reactive. This behavior in a bulk solid is directly analogous to the acid−base rules put forth by Metiu et al. for oxide surfaces,[53] where basic (acidic) surfaces become less basic (acidic) upon adsorption of an acid (base). Varying the H-adsorption location results in significantly different energetic perturbations to the locations of O p-band centers across the full oxide. Furthermore, because of the adsorption of hydrogen, the site of intercalation always becomes the least basic. Finally, the overall heterogeneity in band center energies also changes depending on the site of intercalation, as illustrated by standard deviations depicted as error bars in the left-hand side of Figure 3c. Analogous behavior was observed for the W d-band centers, O Bader charges, and W Bader charges and can be determined for representative configurations across all stoichiometries of H_xWO_3.

The results shown in Figure 3 illustrate that even a modest number of complete electronic structure calculations provides a wealth of information about the site-specific acid−base properties of H_xWO_3 with a given H stoichiometry. We leveraged the availability of this information to examine the extent to which these properties correlate with DFT-calculated hydrogen BE. Figure 4 details descriptor correlation and linear screening model performance. The data shown are for the conversion of $H_{0.125}WO_3$ to $H_{0.250}WO_3$.

The correlation matrix shown in Figure 4a compiles the pairwise PCCs for all 12 acid−base metrics and the DFT-calculated BE. This type of coefficient ranges from −1 to 1 and indicates the linearity of the correlation between the paired quantities. A value of zero indicates the absence of a linear correlation, while a value of −1 or 1 corresponds to exact linearity. It is important to note that while the sign of the coefficient indicates the direction of correlation, the magnitude only indicates the degree of linearity and not the constant of proportionality.

As an illustrative example, the first column of the matrix in Figure 4a gives the correlations for the DFT BE with each candidate descriptor. The averaged neighboring W atoms' d-band centers are negatively correlated with energy: as they become more positive (less acidic), hydrogen binding becomes more preferable. The O p-band centers are also negatively correlated with energy: as the centers become more positive (more basic), hydrogen binding becomes more exothermic. These relationships suggests that the hydrogen prefers sites that are more basic overall, which is analogous to the observed relationship between d-band occupancies and adsorbate BE on pure metal surfaces.[63] Revisiting Figure 3, then, it is apparent that a single O atom most likely binds only one H atom, as the adsorption site then becomes significantly less basic than other sites in the oxide.

While the correlations shown in Figure 4 contain dense information about the physical implications of hydrogen uptake, our primary interest was in using them to select appropriate descriptors for the linear screening models. As can be seen, only five of the descriptors exhibit significant ($|PCC| > 0.55$) linear relationships with the DFT BE. Of these, we selected only the three "before" descriptors to help accelerate screening. This is because using the "after" intercalation descriptors would require DFT calculations to be performed to collect parameters for the model, thereby erasing the computational cost savings when using this data-driven approach. Accordingly, the three features we used were O p-band centers, W d-band centers, and W Bader charges, all before intercalation. These three were used in all screening models. Table 2 details the coefficients and intercepts determined for each H-stoichiometry in H_xWO_3.

Moving across the rows in Table 2, the magnitudes and signs of the β_i values vary significantly, indicating the relationship between hydrogen BE and each individual feature varies with composition. Rather than fit our acid−base model to the global dataset, splitting according to composition allowed for localization of each model. This local approach has been shown to improve the prediction accuracy of models trained on imbalanced data sets[64] and was employed here to capture the effect of composition on each β_i. Furthermore, this local approach helps avoid a reversal paradox[65] encountered in evaluating energy versus composition data for intercalating systems. Figure S5 in the Supporting Information compares the efficacy of using the global versus local data for model training.

The performance of the $H_{0.250}WO_3$ model is depicted in Figure 4b. Importantly, the general trend in energies is captured well by the screening model, highlighting its ability to identify the most exothermic H binding sites. Figure 4c shows the model-predicted hydrogen BE at each oxygen site. Intercalation at the site of the previous H adsorption, O_{14}, is predicted to be endothermic by the model, recapitulating the prior observation that binding multiple units of H to a single site is thermodynamically unfavorable. BEs at every other site are predicted to be exothermic and fall within a range of −0.6 to −0.2 eV. The orange circle shows the most exothermic site according to DFT. The cyan line shows the cutoff point for a follow-up DFT analysis: for sites below the cutoff line that had not been previously subjected to a DFT calculation (i.e., they did not appear in the testing or training data), an additional, explicit calculation was performed.

As noted previously, when hydrogen intercalates into WO_3, there are many sites (O atoms) where the H can reside. Figure

https://dx.doi.org/10.1021/acsami.0c11300
ACS Appl. Mater. Interfaces 2020, 12, 44658−44670

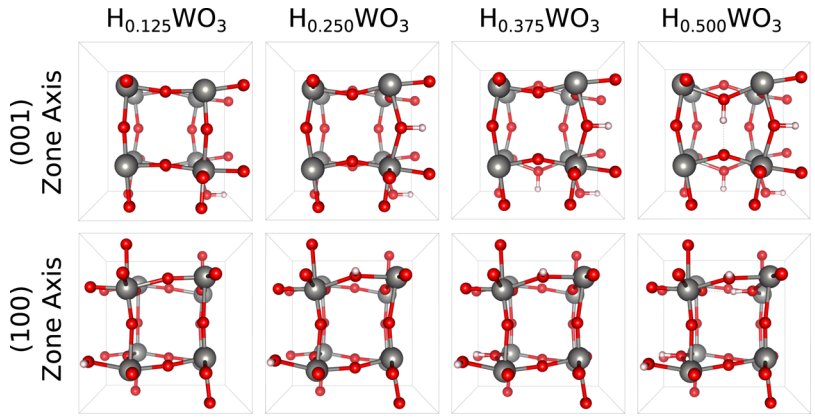

Figure 5. Most exothermic configurations for x = 0.125, 0.250, 0.375, and 0.500 in H_xWO_3 unit cells, increasing from left to right. The first row shows the (001) zone axis, and the second row shows the (100) zone axis. The ordering observed in the (001) axis suggests hydrogen intercalation occurs via staging.

5 shows the most exothermic configurations for the H/W ratios of 0.125, 0.250, 0.375, and 0.500. Interestingly, our data suggest that H intercalation in H_xWO_3 follows a staging process akin to lithium intercalation in carbon-based battery materials.[66] When viewing along the (001) zone axis, hydrogen atoms first fill the right-most channel, then the center channel. Viewed along the (100) axis, the atoms populate the cell alternating between the lower and center channels. Thus, it is apparent that hydrogen tends to intercalate in WO_3 in an ordered manner, as revealed through the most exothermic configurations identified by our linear models.

While the linear screening models were successful at identifying trends in hydrogen BE, they did not achieve sufficient accuracy for comparison to experimental results. To improve the accuracy of the predicted H intercalation energies, we constructed a second statistical model using KRR. This model took the most stable configuration at each stoichiometry (identified by the linear models) as an input and predicted the BE for the next unit of hydrogen at every O site. Figure 6 shows the performance of the KRR model as a parity plot that compares the associated predictions with the DFT-calculated BE. Hyperparameter tuning for the KRR model is further discussed in the Supporting Information and shown in Figure S6.

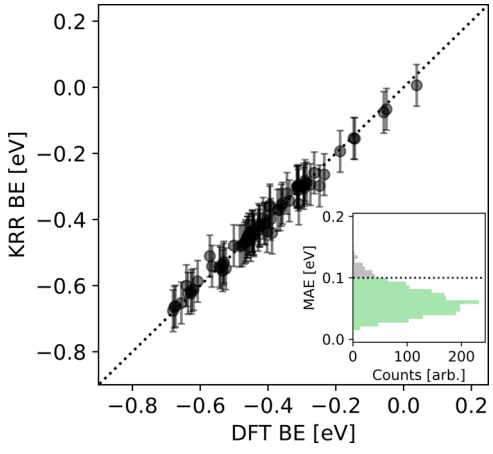

Figure 6. Parity plot demonstrating performance of the acid−base KRR model. Error bars are drawn as ±0.063 eV, which was the average MAE resulting from repeated 10-fold cross-validation. The inset is the null distribution of MAE values formed from each model created during cross-validation, with the dotted line demarcating a nominal accuracy limit of 0.10 eV. 94% of all models generated in cross-validation exhibited MAEs lower than this threshold.

The KRR model includes the same three descriptors used in the screening stage as well as the initial O Bader charge and the H-stoichiometry itself. Repeated 10-fold cross validation showed an average model MAE of 0.063 eV, illustrated by the inset of Figure 6. 94% of all models exhibited an MAE lower than 0.10 eV, therefore we can say that the parameterized KRR model is accurate to 0.10 eV with a p-value of 0.06. One of the biggest differences between the linear models and this KRR model is the local versus global approach. The global analysis here performs well because KRR is not restricted to linear correlations, but can effectively capture non-linear behavior. Regularization also helps limit the variance in predictions by the KRR model, where the linear models are not regularized.

KRR model results for H_xWO_3 at all of the modeled stoichiometries are compiled in Table 3. The most exothermic DFT-calculated BE (DFT BE) and most exothermic KRR model-predicted BE (KRR BE) for each stoichiometry are shown, along with the expectation energies calculated via Boltzmann weighting of all O site KRR predictions (expectation BE). DFT intercalation potentials (DFT potential) were then calculated from the most exothermic BEs per the convex hull formulation, whereas the KRR model-predicted intercalation potentials (KRR potential) were calculated from the expectation BE. Notably, the deviations between the DFT and KRR BE do not exceed 0.021 eV, again demonstrating the ability of KRR to capture the relationship between acidity, basicity, and hydrogen BE.

Figure 7 depicts the complete set of hydrogen BE predictions that resulted from the KRR model. The convex energy hull (solid black line in Figure 7a) considers only the lowest energy configurations. However, this approach does not consider that a system with finite thermal energy may access energy states that are above the minimum and will likely do so according to a Boltzmann distribution. This can be addressed by using the full KRR dataset to generate expectation values according to eqs 2 and 3 (orange dots in Figure 7a), which results in predicted hydrogen BE that are slightly higher (less negative) than the most exothermic case. Further application

https://dx.doi.org/10.1021/acsami.0c11300
ACS Appl. Mater. Interfaces 2020, 12, 44658−44670

Table 3. KRR Model Predictions Compared to DFT-Calculated Value Results, All in eV

energy type	$H_{0.125}WO_3$	$H_{0.250}WO_3$	$H_{0.375}WO_3$	$H_{0.500}WO_3$	$H_{0.625}WO_3$
DFT BE	−0.457	−0.680	−0.641	−0.608	−0.427
KRR BE	−0.445	−0.676	−0.623	−0.587	−0.414
expectation BE	−0.437	−0.667	−0.610	−0.569	−0.395
DFT potential	0.457	0.223	−0.040	−0.033	−0.180
KRR potential	0.437	0.229	−0.057	−0.040	−0.175

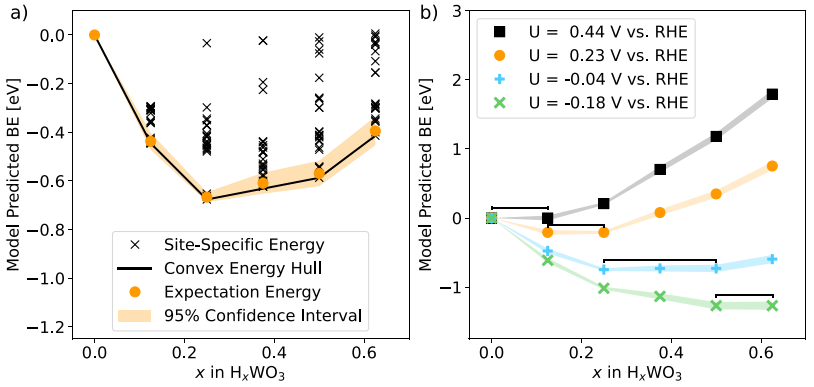

Figure 7. (a) Hydrogen BE predictions for 24 configurations of each stoichiometry. Both the lowest energy convex hull and expectation energy interpretations of the data are shown. The shaded area constitutes the 95% confidence interval on the expectation BE. (b) Effect of applying a potential on H_xWO_3. Equilibrium intercalation potentials were taken as the value of U that causes a given increase in stoichiometry to be thermoneutral. The black brackets indicate the neutral step at each applied potential.

of Boltzmann probabilities enables a confidence interval to be assigned to the expectation value (shaded area in Figure 7a).

These energy versus composition curves can be interpreted as reaction coordinate diagrams, where the transition from one composition to the next corresponds to a PCET reaction for a unit cell of H_xWO_3 intercalating an additional unit of hydrogen. Accordingly, applying the CHE formulation enables us to account for the influence of applied potential, as shown in Figure 7b. The equilibrium potential for a given reaction step can be found by varying the applied potential until the step of interest becomes thermoneutral, as indicated by the black brackets. For example, these data predict that the initial transition from WO_3 to $H_{0.125}WO_3$ has an equilibrium reduction potential of 0.44 V versus RHE.

Interestingly, our calculations show that $H_{0.250}WO_3$, $H_{0.375}WO_3$, and $H_{0.500}WO_3$ are equally stable at an applied potential of −0.04 V versus RHE. This suggests that $H_{0.250}WO_3$ can be directly reduced to $H_{0.500}WO_3$ without forming the intermediate $H_{0.375}WO_3$ as a thermodynamically stable compound. Furthermore, a large number of $H_{0.125}WO_3$ states are situated only slightly above the convex hull. Accordingly, if H-intercalation via the minimum-energy path exhibits a significant activation energy, it is plausible that WO_3 forms $H_{0.250}WO_3$ with no stable $H_{0.125}WO_3$ phase by passing through these higher energy states. As noted above, hydrogen staging in H_xWO_3 also occurs in increments of 2 H atoms per channel in the unit cell, corresponding to a stoichiometric increment of 0.250. These observations suggest hydrogen population in WO_3 may follow a compositional pathway of WO_3 to $H_{0.250}WO_3$ to $H_{0.500}WO_3$ to $H_{0.625}WO_3$, which is consistent with the experimental observations discussed below.

With computational predictions of equilibrium electrochemical potentials in hand, it is possible to compare theory to experiment. Figure 8 shows a representative cyclic voltammogram of WO_3 in N_2-saturated 0.5 M H_2SO_4 (aq) overlaid with the predicted equilibrium potentials shown in Figure 7b.

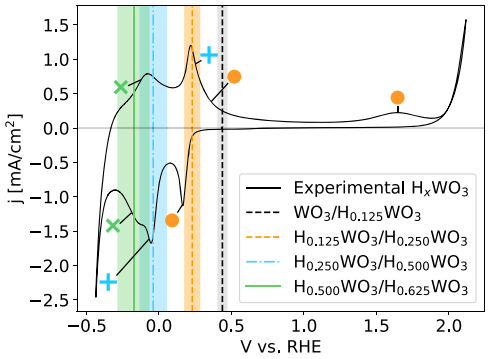

Figure 8. Experimental cyclic voltammogram of H_xWO_3 in 0.5 M H_2SO_4 electrolyte compared to predicted intercalation potentials. The vertical lines show the KRR-predicted intercalation potentials, with the shaded areas showing associated 95% confidence intervals. The symbols further demarcate pairwise assignments of redox features corresponding to H-intercalation and deintercalation. This scan was performed at a 1 mV/s sweep rate.

Several redox features were observed in the potential range from −0.5 to 2.2 V versus RHE. These negative and positive limits were dictated, respectively, by the hydrogen evolution reaction (HER) and the oxygen evolution reaction (OER), both of which can be accessed by H_xWO_3 without irreversible degradation. The voltammetric features related to H-intercalation and deintercalation are labeled with colored symbols, along with the Nernst equilibrium potentials predicted by the KRR model.

We observed at least three distinct H-intercalation events in the voltammograms, and each of these exhibited nonzero peak-to-peak separation at scan rates as low as 1 mV/s. This is

https://dx.doi.org/10.1021/acsami.0c11300
ACS Appl. Mater. Interfaces 2020, 12, 44658−44670

consistent with kinetic and/or mass transfer limitations, which are known for anhydrous H_xWO_3.[19] Nonetheless, the equilibrium potential for the associated intercalation/de-intercalation reactions must be located between the respective positive and negative peak currents. Accordingly, the predicted equilibrium potential ranges (i.e., expectation values ±95% confidence intervals) for each redox couple—WO_3/$H_{0.250}WO_3$, $H_{0.250}WO_3$/$H_{0.500}WO_3$, and $H_{0.500}WO_3$/$H_{0.625}WO_3$—agree with the observed features.

The peak assignments are further justified by UV−vis measurements shown in Figure S7. These data show increased absorption across the optical spectrum, confirming the darkening of the film expected with the electrochromism of bronze formation. Tauc plots of the films polarized to various degrees of intercalation also show a loss of semiconducting character, in line with the EIS measurements shown below. Hydrogen insertion also perturbs the crystal structure of WO_3, as evidenced by the XRD results in Figure S8 that indicate a progressive increase in crystal symmetry.

The equilibrium potential for the WO_3/$H_{0.125}WO_3$ redox couple is noticeably unpaired with any features observed in the CV. This observation further supports the notion that $H_{0.125}WO_3$ formation is kinetically sluggish, resulting in the direct formation of $H_{0.250}WO_3$ from WO_3. Beyond the low-lying metastable states that may offer a direct path from WO_3 to $H_{0.250}WO_3$, it is possible that the limited electronic conductivity in bare WO_3 also hinders the rate of electron transfer. Consequently, high overpotentials are needed to drive WO_3 to $H_{0.125}WO_3$, and it is plausible that they are high enough to overlap with the onset of $H_{0.250}WO_3$ formation. Intercalation onset overpotentials in this case could also be attributable not to reaction kinetics, but instead to the least negative potential that is required to raise the Fermi level of WO_3 above the conduction band minimum (i.e., to place the semiconductor into strong forward bias).

These data also provide a plausible explanation for why $H_{0.500}WO_3$ is frequently observed as the maximum H-stoichiometry in laboratory experiments.[13] The equilibrium potential for the $H_{0.250}WO_3$/$H_{0.500}WO_3$ couple is modestly negative of 0 V versus RHE, which means that increasingly negative applied potentials increase the driving force for the HER. Hence, hydrogen evolution likely competes directly with the formation of higher bronze stoichiometries. Specifically, we speculate that $H_{0.625}WO_3$ is unstable toward decomposition via hydrogen evolution, where the reaction product is $H_{0.500}WO_3$, as has been suggested previously.[67]

Figure 9 presents a set of "window-opening" experiments over the potential range encompassing only the initial H-intercalation events. Considering the positions of the redox features and the composition versus energy profile shown in Figure 7, peaks I and IV apparently correspond to the formation of $H_{0.250}WO_3$ and $H_{0.500}WO_3$, respectively. The expected ratio of IV/I integrated areas is thus 1:1. We observe a slightly larger ratio of 1.41:1 that nonetheless supports the assignments made in Figure 8. The extra charge could perhaps result from overlap between $H_{0.625}WO_3$ reduction and peak IV, which might contribute charge injection beyond the $x = 0.500$ composition. Peak IV also occurs negative of 0.0 V versus RHE, and so we also cannot rule out additional charge from background hydrogen evolution.

In another intriguing observation, we identified two oxidation features that could be paired with the WO_3/$H_{0.250}WO_3$ redox couple: one at ∼0.25 V versus RHE and another at a much more positive potential of ∼1.7 V versus RHE. Peak I corresponds to the initial H-intercalation event; reversing the voltammetric scan at 0.07 V versus RHE results in two oxidation features, labeled II and III. The control experiment shown in Figure S9, where the CV was initiated as a positive-going sweep starting with no intercalated hydrogen, suggests that peak III is not because of the electrode substrate or adventitious contaminants. Moreover, peak II is not large enough to constitute full removal of H from $H_{0.250}WO_3$, and we observed that the distinctive blue coloration of H_xWO_3 was only fully converted back to the initial pale yellow/green upon cycling to large positive potentials or allowing the sample to stand in air for at least several minutes. Hence, although a small overpotential is required to initiate deintercalation of hydrogen from $H_{0.250}WO_3$, a much larger positive bias is required to fully deintercalate the bronze.

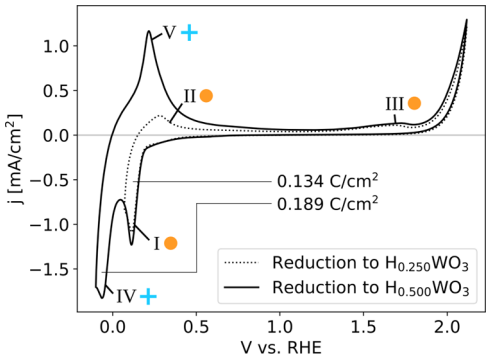

Figure 9. Window-opening CV over the first and second intercalation events showing the irreversible charge−discharge behavior of low H-content H_xWO_3 and the corresponding oxidation feature at ∼1.7 V versus RHE. These scans were performed at 1 mV/s.

We postulate that the irreversibility of intercalation is not primarily attributable to classical electron-transfer kinetics, but instead to the distinct difference in electronic conductivity between WO_3 and H_xWO_3. It is well established that H-intercalation in WO_3 induces a semiconductor-to-metal transition;[68] accordingly, deintercalation leads to a transition from a metallic state to a semiconducting one. This may give rise to the situation schematized in Figure 10a, where the final units of hydrogen in H_xWO_3 ($x < 0.250$) become isolated from the substrate by a layer of semiconducting WO_3. This "stranded" hydrogen would only then be removed from the bronze upon application of a sufficiently large overvoltage to induce electromigration of the remaining H units and/or dielectric breakdown of the oxide layer. Similar observations of irreversibility have been previously made for lithium ion trapping in WO_3.[69]

The irreversible coloration of the film could also be because of the loss of lattice oxygen and the formation of substoichiometric WO_{3-x}.[70] Although this is plausible, we observe a full return to the yellow-green color of the original oxide if samples are left in ambient air. Because gain or loss of lattice oxygen involves multiple electron transfers, we do not expect ambient oxygen to convert WO_{3-x} to WO_3 at an appreciable rate; we therefore conclude that the trapping of hydrogen equivalents is responsible for the irreversibility of film coloration. Further studies to understand this effect are warranted, as this type of irreversibility presents a challenge when using WO_3 in energy storage, optoelectronics, or redox catalysis.

https://dx.doi.org/10.1021/acsami.0c11300
ACS Appl. Mater. Interfaces 2020, 12, 44658−44670

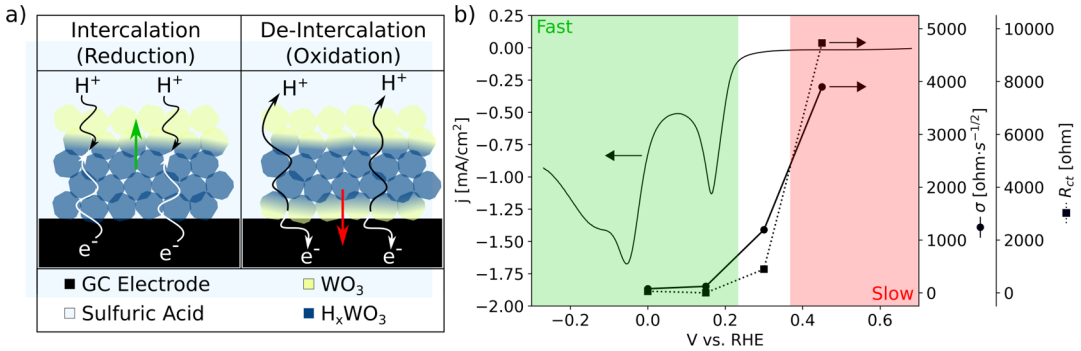

Figure 10. (a) Illustration of the stranding effect that may result from the metal-to-semiconductor transition in H_xWO_3 ($x < 0.250$) upon hydrogen removal and (b) EIS fit parameters demonstrating significant mass and charge-transfer limitations for nonintercalated bronze.

Figure 10b shows the results of fitting a Randles circuit to impedance data taken at various potentials. The raw data and fits are shown in Figure S10 of the Supporting Information. It is clear that the parent WO_3 exhibits a large charge-transfer resistance (R_{ct}) and appreciable mass transfer limitations for charge transfer (Warburg coefficient, σ). Polarization to potentials that coincide with H-intercalation results in a drastic reduction in both of these parameters, suggesting that charge transfer is much faster in bronzes than in the pure oxide. Interestingly, the reduction in σ and R_{ct} begins even positive of the initial intercalation (peak I in Figure 9) at ∼0.30 V versus RHE. We also observed an initial small cathodic current upon polarization of the sample at 0.3 V versus RHE prior to collecting the impedance data. This leads us to believe that the improved charge-transfer rate is related to either a small amount of charge accumulation at the nanoparticle−electrolyte interface or near-surface proton reduction. Regardless, the EIS data clearly show that WO_3 and H_xWO_3 are characterized by vastly different charge-transfer dynamics.

5. CONCLUSIONS

We have introduced a computational framework to predict and rationalize hydrogen intercalation thermodynamics in H_xWO_3 using acid−base properties that can be readily calculated with computationally inexpensive DFT methods. Pair-wise correlations between hydrogen BE, DOS, and Bader charges revealed an intimate relationship between acidity, basicity, and hydrogen intercalation energies that is broadly indicative of the reaction as PCET. By applying data science methods, we predicted the most stable atomic configurations and the associated hydrogen BE in H_xWO_3 using an accelerated scheme that replaces large-scale DFT calculations with targeted ones based on statistical regression. The additional application of Boltzmann statistics to each of these predicted intercalation configurations enabled us to calculate expectation values and physically meaningful confidence intervals for the equilibrium potentials of H-intercalation reactions. The resulting predictions agreed with experiments, both in terms of the total number of distinct redox events and their onset potentials. Electrochemical measurements on crystalline H_xWO_3 also evidenced significant irreversibility for H-intercalation at low hydrogen stoichiometries, possibly because of electronic conductivity limitations associated with the known semiconductor-to-metal transition in this hydrogen bronze.

In summary, this work provides valuable insights into factors that influence hydrogen uptake in WO_3 across the full range of experimentally accessible H-stoichiometries. More broadly, we have introduced a computational framework that can be applied to other oxide bronze materials to elucidate the composition-dependent energetics of hydrogen intercalation. Our work outlines a pathway for accelerated computational materials discovery of redox-active metal oxides of interest for applications in catalysis and energy storage.

■ ASSOCIATED CONTENT

Supporting Information

The Supporting Information is available free of charge at https://pubs.acs.org/doi/10.1021/acsami.0c11300.

Comparison of nanoparticle and thin film WO_3, investigation of electronic structure makeup, PBE-D3 and HSE06 DOS comparison, further details on linear/KRRs, window-opening control experiment, composition-dependent ex situ UV−vis and XRD measurements, EIS data fitting, scan rate and anion effects on voltammetry data, and confirmation of the disk-like nanoparticle morphology (PDF)

■ AUTHOR INFORMATION

Corresponding Authors

Giannis Mpourmpakis − *Department of Chemical & Petroleum Engineering, University of Pittsburgh, Pittsburgh, Pennsylvania 15260, United States;* orcid.org/0000-0002-3063-0607; Email: gmpourmp@pitt.edu

James R. McKone − *Department of Chemical & Petroleum Engineering, University of Pittsburgh, Pittsburgh, Pennsylvania 15260, United States;* orcid.org/0000-0001-6445-7884; Email: jmckone@pitt.edu

Author

Evan V. Miu − *Department of Chemical & Petroleum Engineering, University of Pittsburgh, Pittsburgh, Pennsylvania 15260, United States;* orcid.org/0000-0003-0429-5101

Complete contact information is available at: https://pubs.acs.org/10.1021/acsami.0c11300

Notes

The authors declare no competing financial interest.

■ ACKNOWLEDGMENTS

E.V.M. acknowledges support from the National Science Foundation Graduate Research Fellowship Program under grant no. 1747452. G.M. acknowledges support from the National Science Foundation under grant no. 1920623. J.R.M. acknowledges support from the Arnold and Mabel Beckman

Foundation. This research was also supported by the Center for Research Computing, the Swanson School of Engineering, and the Mascaro Center for Sustainable Innovation at the University of Pittsburgh.

■ ABBREVIATIONS

DFT, density functional theory
CV, cyclic voltammetry
WO_3, tungsten trioxide

■ REFERENCES

(1) Hersh, H. N.; Kramer, W. E.; McGee, J. H. Mechanism of Electrochromism in WO3. *Appl. Phys. Lett.* **1975**, *27*, 646−648.
(2) Jiao, Z.; Wang, J.; Ke, L.; Liu, X.; Demir, H. V.; Yang, M. F.; Sun, X. W. Electrochromic Properties of Nanostructured Tungsten Trioxide (Hydrate) Films and Their Applications in a Complementary Electrochromic Device. *Electrochim. Acta* **2012**, *63*, 153−160.
(3) Penza, M.; Tagliente, M. A.; Mirenghi, L.; Gerardi, C.; Martucci, C.; Cassano, G. Tungsten Trioxide (WO3) Sputtered Thin Films for a NOx Gas Sensor. *Sens. Actuators, B* **1998**, *50*, 9−18.
(4) Lin, H.-M.; Hsu, C.-M.; Yang, H.-Y.; Lee, P.-Y.; Yang, C.-C. Nanocrystalline WO3-based H2S Sensors. *Sens. Actuators, B* **1994**, *22*, 63−68.
(5) Li, W.-J.; Fu, Z.-W. Nanostructured WO3 Thin Film as a New Anode Material for Lithium-ion Batteries. *Appl. Surf. Sci.* **2010**, *256*, 2447−2452.
(6) Huang, K.; Pan, Q.; Yang, F.; Ni, S.; Wei, X.; He, D. Controllable Synthesis of Hexagonal WO3 Nanostructures and Their Application in Lithium Batteries. *J. Phys. D: Appl. Phys.* **2008**, *41*, 155417−155422.
(7) Jayaraman, S.; Jaramillo, T. F.; Baeck, S.-H.; McFarland, E. W. Synthesis and Characterization of Pt-WO3 as Methanol Oxidation Catalysts for Fuel Cells. *J. Phys. Chem. B* **2005**, *109*, 22958−22966.
(8) Shen, P. K.; Tseung, A. C. C. Anodic Oxidation of Methanol on Pt/WO3 in Acidic Media. *J. Electrochem. Soc.* **1994**, *141*, 3082−3090.
(9) Tseung, A. C. C.; Shen, P. K.; Chen, K. Y. Precious Metal/Hydrogen Bronze Anode Catalysts for the Oxidation of Small Organic Molecules and Impure Hydrogen. *J. Power Sources* **1996**, *61*, 223−225.
(10) Kim, J. H.; Magesh, G.; Kang, H. J.; Banu, M.; Kim, J. H.; Lee, J.; Lee, J. S. Carbonate-Coordinated Cobalt co-Catalyzed BiVO4/WO3 Composite Photoanode Tailored for CO2 Reduction to Fuels. *Nano Energy* **2015**, *15*, 153−163.
(11) Jin, J.; Yu, J.; Guo, D.; Cui, C.; Ho, W. A Hierarchical Z-scheme CdS−WO3 Photocatalyst with Enhanced CO2 Reduction Activity. *Small* **2015**, *11*, 5262−5271.
(12) Glemser, O.; Sauer, H. Die Zusammensetzung von Wolframblau. *Z. Anorg. Chem.* **1943**, *252*, 160−163.
(13) Sermon, P. A.; Bond, G. C. Studies of Hydrogen Spillover. Part 4.−Factors Affecting Hydrogen Spillover and its Reversal. *J. Chem. Soc., Faraday Trans. 1* **1980**, *76*, 889−900.
(14) Machida, K. i.; Enyo, M. Structural and Electrochromic Properties of Tungsten and Molybdenum Trioxide Electrodes in Acidic Media. *J. Electrochem. Soc.* **1990**, *137*, 1169−1175.
(15) Magnéli, A.; Blomberg, B.; Reio, L.; Saluste, E.; Stjernholm, R.; Ehrensvärd, G. Contribution to the Knowledge of the Alkali Tungsten Bronzes. *Acta Chem. Scand.* **1951**, *5*, 372−378.
(16) Bohnke, O.; Robert, G. Electrochemical Lithium Incorporation into WO3 and MoO3 Thin Films. *Solid State Ionics* **1982**, *6*, 115−120.
(17) He, Y.; Gu, M.; Xiao, H.; Luo, L.; Shao, Y.; Gao, F.; Du, Y.; Mao, S. X.; Wang, C. Atomistic Conversion Reaction Mechanism of WO3 in Secondary Ion Batteries of Li, Na, and Ca. *Angew. Chem., Int. Ed.* **2016**, *55*, 6244−6247.
(18) Mitchell, J. B.; Lo, W. C.; Genc, A.; LeBeau, J.; Augustyn, V. Transition from Battery to Pseudocapacitor Behavior via Structural Water in Tungsten Oxide. *Chem. Mater.* **2017**, *29*, 3928−3937.
(19) Mitchell, J. B.; Geise, N. R.; Paterson, A. R.; Osti, N. C.; Sun, Y.; Fleischmann, S.; Zhang, R.; Madsen, L. A.; Toney, M. F.; Jiang, D.-e.; Kolesnikov, A. I.; Mamontov, E.; Augustyn, V. Confined Interlayer Water Promotes Structural Stability for High-Rate Electrochemical Proton Intercalation in Tungsten Oxide Hydrates. *ACS Energy Lett.* **2019**, *4*, 2805−2812.
(20) Miu, E. V.; McKone, J. R. Comparisons of WO3 Reduction to HxWO3 Under Thermochemical and Electrochemical Control. *J. Mater. Chem. A* **2019**, *7*, 23756−23761.
(21) Yan, B.; Bisbey, R. P.; Alabugin, A.; Surendranath, Y. Mixed Electron−Proton Conductors Enable Spatial Separation of Bond Activation and Charge Transfer in Electrocatalysis. *J. Am. Chem. Soc.* **2019**, *141*, 11115−11122.
(22) Peper, J. L.; Mayer, J. M. Manifesto on the Thermochemistry of Nanoscale Redox Reactions for Energy Conversion. *ACS Energy Lett.* **2019**, *4*, 866−872.
(23) Ingham, B.; Hendy, S.; Chong, S.; Tallon, J. Density-Functional Studies of Tungsten Trioxide, Tungsten Bronzes, and Related Systems. *Phys. Rev. B: Condens. Matter Mater. Phys.* **2005**, *72*, 075109.
(24) Di Valentin, C.; Wang, F.; Pacchioni, G. Tungsten Oxide in Catalysis and Photocatalysis: Hints from DFT. *Top. Catal.* **2013**, *56*, 1404−1419.
(25) Wang, F.; Di Valentin, C.; Pacchioni, G. DFT Study of Hydrogen Adsorption on the Monoclinic WO3 (001) Surface. *J. Phys. Chem. C* **2012**, *116*, 10672−10679.
(26) Lin, H.; Zhou, F.; Liu, C.-P.; Ozoliņš, V. Non-Grotthuss Proton Diffusion Mechanism in Tungsten Oxide Dihydrate from First-Principles Calculations. *J. Mater. Chem. A* **2014**, *2*, 12280−12288.
(27) Xi, Y.; Zhang, Q.; Cheng, H. Mechanism of Hydrogen Spillover on WO3 (001) and Formation of H x WO3 (x= 0.125, 0.25, 0.375, and 0.5). *J. Phys. Chem. C* **2014**, *118*, 494−501.
(28) Urban, A.; Seo, D.; Ceder, G. Computational Understanding of Li-ion Batteries. *npj Comput. Mater.* **2016**, *2*, 16010.
(29) Jain, A.; Hautier, G.; Moore, C.; Kang, B.; Lee, J.; Chen, H.; Twu, N.; Ceder, G. A Computational Investigation of Li9M3 (P2O7) 3 (PO4) 2 (M= V, Mo) as Cathodes for Li ion Batteries. *J. Electrochem. Soc.* **2012**, *159*, A622−A633.
(30) Hautier, G.; Jain, A.; Chen, H.; Moore, C.; Ong, S. P.; Ceder, G. Novel Mixed Polyanions Lithium-ion Battery Cathode Materials Predicted by High-Throughput Ab Initio Computations. *J. Mater. Chem.* **2011**, *21*, 17147−17153.
(31) Kresse, G.; Furthmüller, J. Efficient Iterative Schemes for Ab Initio Total-Energy Calculations Using a Plane-Wave Basis Set. *Phys. Rev. B: Condens. Matter Mater. Phys.* **1996**, *54*, 11169−11186.
(32) Momma, K.; Izumi, F. VESTA 3 for Three-Dimensional Visualization of Crystal, Volumetric and Morphology Data. *J. Appl. Crystallogr.* **2011**, *44*, 1272−1276.
(33) Perdew, J. P.; Burke, K.; Ernzerhof, M. Generalized Gradient Approximation Made Simple. *Phys. Rev. Lett.* **1996**, *77*, 3865−3868.
(34) Grimme, S.; Antony, J.; Ehrlich, S.; Krieg, H. A Consistent and Accurate Ab Initio Parametrization of Density Functional Dispersion Correction (DFT-D) for the 94 Elements H-Pu. *J. Chem. Phys.* **2010**, *132*, 154104−154122.
(35) Grimme, S.; Ehrlich, S.; Goerigk, L. Effect of the Damping Function in Dispersion Corrected Density Functional Theory. *J. Comput. Chem.* **2011**, *32*, 1456−1465.
(36) Lee, Y.; Lee, T.; Jang, W.; Soon, A. Unraveling the Intercalation Chemistry of Hexagonal Tungsten Bronze and its Optical Responses. *Chem. Mater.* **2016**, *28*, 4528−4535.
(37) Hinuma, Y.; Hayashi, H.; Kumagai, Y.; Tanaka, I.; Oba, F. Comparison of Approximations in Density Functional Theory Calculations: Energetics and Structure of Binary Oxides. *Phys. Rev. B* **2017**, *96*, 094102.
(38) Blöchl, P. E.; Jepsen, O.; Andersen, O. K. Improved Tetrahedron Method for Brillouin-Zone Integrations. *Phys. Rev. B: Condens. Matter Mater. Phys.* **1994**, *49*, 16223−16233.
(39) Woodward, P. M.; Sleight, A. W.; Vogt, T. Structure Refinement of Triclinic Tungsten Trioxide. *J. Phys. Chem. Solids* **1995**, *56*, 1305−1315.

https://dx.doi.org/10.1021/acsami.0c11300
ACS Appl. Mater. Interfaces 2020, 12, 44658−44670

(40) Sanville, E.; Kenny, S. D.; Smith, R.; Henkelman, G. Improved Grid-based Algorithm for Bader Charge Allocation. *J. Comput. Chem.* **2007**, *28*, 899−908.
(41) Cholewinski, M. C.; Dixit, M.; Mpourmpakis, G. Computational Study of Methane Activation on γ-Al2O3. *ACS Omega* **2018**, *3*, 18242−18250.
(42) Pedregosa, F.; Varoquaux, G.; Gramfort, A.; Michel, V.; Thirion, B.; Grisel, O.; Blondel, M.; Prettenhofer, P.; Weiss, R.; Dubourg, V.; Vanderplas, J.; Passos, A.; Cournapeau, D.; Brucher, M.; Perrot, M.; Duchesnay, E. Scikit-learn: Machine Learning in Python. *J. Mach. Learn. Res.* **2011**, *12*, 2825−2830.
(43) Nørskov, J. K.; Rossmeisl, J.; Logadottir, A.; Lindqvist, L.; Kitchin, J. R.; Bligaard, T.; Jonsson, H. Origin of the Overpotential for Oxygen Reduction at a Fuel-Cell Cathode. *J. Phys. Chem. B* **2004**, *108*, 17886−17892.
(44) Burkhardt, S.; Elm, M. T.; Lani-Wayda, B.; Klar, P. J. In Situ Monitoring of Lateral Hydrogen Diffusion in Amorphous and Polycrystalline WO3 Thin Films. *Adv. Mater. Interfaces* **2018**, *5*, 1701587−2170195.
(45) Di Paola, A.; Di Quarto, F.; Sunseri, C. Electrochromism in Anodically Formed Tungsten Oxide Films. *J. Electrochem. Soc.* **1978**, *125*, 1344−1347.
(46) Regragui, M.; Addou, M.; Outzourhit, A.; Bernéde, J. C.; El Idrissi, E.; Benseddik, E.; Kachouane, A. Preparation and Characterization of Pyrolytic Spray Deposited Electrochromic Tungsten Trioxide Films. *Thin Solid Films* **2000**, *358*, 40−45.
(47) Shen, P. K.; Huang, H. T.; Tseung, A. C. C. A Study of Tungsten Trioxide and Polyaniline Composite Films I. Electrochemical and Electrochromic Behavior. *J. Electrochem. Soc.* **1992**, *139*, 1840−1845.
(48) Tosoni, S.; Di Valentin, C.; Pacchioni, G. Effect of Alkali Metals Interstitial Doping on Structural and Electronic Properties of WO3. *J. Phys. Chem. C* **2014**, *118*, 3000−3006.
(49) Van der Ven, A.; Aydinol, M. K.; Ceder, G.; Kresse, G.; Hafner, J. First-Principles Investigation of Phase Stability in Li_xCoO_2. *Phys. Rev. B: Condens. Matter Mater. Phys.* **1998**, *58*, 2975−2987.
(50) Wolverton, C.; Zunger, A. First-Principles Prediction of Vacancy Order-Disorder and Intercalation Battery Voltages in Li_xCoO_2. *Phys. Rev. Lett.* **1998**, *81*, 606−609.
(51) Murphy, K. P. *Machine Learning: A Probabilistic Perspective*; MIT Press, 2012.
(52) McFarland, E. W.; Metiu, H. Catalysis by Doped Oxides. *Chem. Rev.* **2013**, *113*, 4391−4427.
(53) Metiu, H.; Chrétien, S.; Hu, Z.; Li, B.; Sun, X. Chemistry of Lewis Acid−Base Pairs on Oxide Surfaces. *J. Phys. Chem. C* **2012**, *116*, 10439−10450.
(54) Chrétien, S.; Metiu, H. Acid−Base Interaction and its Role in Alkane Dissociative Chemisorption on Oxide Surfaces. *J. Phys. Chem. C* **2014**, *118*, 27336−27342.
(55) Kostetskyy, P.; Yu, J.; Gorte, R.; Mpourmpakis, G. Structure−Activity Relationships on Metal-Oxides: Alcohol Dehydration. *Catal. Sci. Technol.* **2014**, *4*, 3861−3869.
(56) Dixit, M.; Kostetskyy, P.; Mpourmpakis, G. Structure-Activity Relationships in Alkane Dehydrogenation on γ-Al2O3: Site-Dependent Reactions. *ACS Catal.* **2018**, *8*, 11570−11578.
(57) Christiansen, M. A.; Mpourmpakis, G.; Vlachos, D. G. Density Functional Theory-Computed Mechanisms of Ethylene and Diethyl Ether Formation from Ethanol on γ-Al_2O_3 (100). *ACS Catal.* **2013**, *3*, 1965−1975.
(58) Warren, J. J.; Tronic, T. A.; Mayer, J. M. Thermochemistry of Proton-coupled Electron Transfer Reagents and its Implications. *Chem. Rev.* **2010**, *110*, 6961−7001.
(59) Dekock, R.; Gray, H. *Chemical Structure and Bonding*; University Science Books, 1989.
(60) Hoffmann, R. *Solids and Surfaces: A Chemists View of Bonding in Extended Structures*; Wiley-VCH, 2002.
(61) Pearson, R. G. Hard and Soft Acids and Bases. *J. Am. Chem. Soc.* **1963**, *85*, 3533−3539.
(62) Krukau, A. V.; Vydrov, O. A.; Izmaylov, A. F.; Scuseria, G. E. Influence of the Exchange Screening Parameter on the Performance of Screened Hybrid Functionals. *J. Chem. Phys.* **2006**, *125*, 224106−224110.
(63) Nilsson, A.; Pettersson, L. G. M.; Hammer, B.; Bligaard, T.; Christensen, C. H.; Nørskov, J. K. The Electronic Structure Effect in Heterogeneous Catalysis. *Catal. Lett.* **2005**, *100*, 111−114.
(64) Haghighatlari, M.; Shih, C.; Hachmann, J. Thinking Globally, Acting Locally: On the Issue of Training Set Imbalance and the Case for Local Machine Learning Models in Chemistry. **2019**; pp 1−10, ChemRxiv:10.26434/chemrxiv.8796947.v1.
(65) Tu, Y.-K.; Gunnell, D.; Gilthorpe, M. S. Simpson's Paradox, Lord's Paradox, and Suppression Effects are the Same Phenomenon−the Reversal Paradox. *Emerg. Themes Epidemiol.* **2008**, *5*, 2.
(66) Kaskhedikar, N. A.; Maier, J. Lithium Storage in Carbon Nanostructures. *Adv. Mater.* **2009**, *21*, 2664−2680.
(67) Dickens, P. G.; Moore, J. H.; Neild, D. J. Thermochemistry of Hydrogen Tungsten Bronze Phases HxWO3. *J. Solid State Chem.* **1973**, *7*, 241−244.
(68) Shanks, H. R.; Sidles, P. H.; Danielson, G. C. Electrical Properties of the Tungsten Bronzes. *Adv. Chem.* **1963**, *39*, 237−245.
(69) Chatzikyriakou, D.; Krins, N.; Gilbert, B.; Colson, P.; Dewalque, J.; Denayer, J.; Cloots, R.; Henrist, C. Mesoporous Amorphous Tungsten Oxide Electrochromic Films: a Raman Analysis of Their Good Switching Behavior. *Electrochim. Acta* **2014**, *137*, 75−82.
(70) Leftheriotis, G.; Papaefthimiou, S.; Yianoulis, P.; Siokou, A. Effect of the Tungsten Oxidation States in the Thermal Coloration and Bleaching of Amorphous WO3 Films. *Thin Solid Films* **2001**, *384*, 298−306.

https://dx.doi.org/10.1021/acsami.0c11300
ACS Appl. Mater. Interfaces 2020, 12, 44658−44670